GDCh

Research Article

Angewandte
Chemie
International Edition
www.angewandte.org

VIP **Photocatalysis** *Very Important Paper*

Oxygen Vacancies Trigger Rapid Charge Transport Channels at the Engineered Interface of S-Scheme Heterojunction for Boosting Photocatalytic Performance

Di Zu[+], Yiran Ying[+], Qi Wei, Pei Xiong, Mortuza Saleque Ahmed, Zezhou Lin,
Molly Meng-Jung Li, Mingjie Li, Zhihang Xu, Gao Chen, Liqi Bai, Sixuan She,
Yuen Hong Tsang,* and Haitao Huang*

Abstract: Although oxygen vacancies (Ovs) have been intensively studied in single semiconductor photocatalysts, exploration of intrinsic mechanisms and in-depth understanding of Ovs in S-scheme heterojunction photocatalysts are still limited. Herein, a novel S-scheme photocatalyst made from WO_3-Ov/In_2S_3 with Ovs at the heterointerface is rationally designed. The microscopic environment and local electronic structure of the S-scheme heterointerface are well optimized by Ovs. Femtosecond transient absorption spectroscopy (fs-TAS) reveals that Ovs trigger additional charge movement routes and therefore increase charge separation efficiency. In addition, Ovs have a synergistic effect on the thermodynamic and kinetic parameters of S-scheme photocatalysts. As a result, the optimal photocatalytic performance is significantly improved, surpassing that of single component WO_3-Ov and In_2S_3 (by 35.5 and 3.9 times, respectively), as well as WO_3/In_2S_3 heterojunction. This work provides new insight into regulating the photogenerated carrier dynamics at the heterointerface and also helps design highly efficient S-scheme photocatalysts.

[*] Dr. D. Zu,[+] Dr. Y. Ying,[+] Dr. Q. Wei, Dr. P. Xiong, Dr. M. S. Ahmed, Dr. Z. Lin, Dr. M. M.-J. Li, Dr. M. Li, Dr. Z. Xu, Dr. G. Chen, Dr. L. Bai, Dr. S. She, Prof. Y. H. Tsang, Prof. H. Huang
Department of Applied Physics and Materials Research Center, The Hong Kong Polytechnic University, Hung Hom, Kowloon, Hong Kong
E-mail: yuen.tsang@polyu.edu.hk
aphhuang@polyu.edu.hk

Dr. M. S. Ahmed, Prof. Y. H. Tsang
Photonics Research Institute, The Hong Kong Polytechnic University, Hung Hom, Kowloon, Hong Kong

Prof. Y. H. Tsang
Shenzhen Research Institute, The Hong Kong Polytechnic University, 518057 Shenzhen, Guangdong, People's Republic of China

[+] These authors contributed equally to this work.

Introduction

Photocatalysis offers a green and sustainable method of converting solar energy to chemical energy with high values, and it has the potential to be an important tool in the fight against climate change and other energy and environmental crises.[1–3] The photocatalytic process of semiconductor-based photocatalysts typically consists of the following three stages: 1) photoexcitation-induced charge generation; 2) charge transfer from bulk to the surface of photocatalysts; 3) redox reaction of photogenerated charges with adsorbed molecules on the surface.[4] The efficiencies of the three steps jointly determine the overall efficiency of semiconductor photocatalyst. The wide band gap ensures redox capacity of photogenerated carriers, but weakens light-absorption ability, creating an inherent paradox for a single semiconductor photocatalyst.[5] Moreover, the photogenerated electrons and holes are prone to recombine, which severely hinders photocatalytic performance.[6–8]

S-scheme photocatalysts, as the most potential heterojunction structure, shows great advantage in optimizing the charge separation efficiency and enhancing the photocatalytic performance.[9–10] It has been proved that S-scheme photocatalyst can achieve efficient spatial charge separation and high redox potentials of photogenerated carriers simultaneously, which are hard to implement in other types of heterojunctions.[11–12] Generally, a S-scheme heterojunction is composed of an oxidation photocatalyst (OP) with a more positive valence band (VB) and a reduction photocatalyst (RP) with a more negative conduction band (CB). When they come into contact, Fermi level (E_f) difference acts as a driving force, causing electrons to move from RP to OP, resulting in the formation of an internal electric field. After being irradiated, the photogenerated electrons in CB of OP merge with photogenerated holes in VB of RP through this internal electric field. As a result, photogenerated electrons in the CB of RP and the holes in the VB of OP with strong redox abilities are conserved and may participate in photocatalytic reactions.[9] It is worth mentioning that the interface regulation of S-scheme is crucial, in which the charge transfer and separation occurs.

Oxygen vacancies (Ovs) as a type of intrinsic defects can adjust the local geometric structure of metal oxides, thus tailoring the physical and chemical properties of metal oxide

photocatalysts.[13–15] Ovs can alter the band alignment of metal oxides and generate the defect level,[16–17] which play an important role in light absorption.[4,14] Meanwhile, the generation of Ovs in photocatalysts leads to changes in charge separation and transfer process.[14] Although the role of Ovs in single component semiconductors has been extensively studied, their modulation mechanism on hetero-junction structures, especially in S-scheme heterointerface, lacks in-depth exploration and understanding. Hence, it is highly desirable to unravel the function of Ovs completely at the heterointerface of S-scheme, which may not only bring out the potential of Ovs into S-scheme photocatalysts, but also is beneficial for developing photocatalysts with superior performance.

Herein, a series of novel WO_3-Ov/In_2S_3 S-scheme heterojunction photocatalysts were successfully fabricated, in which Ovs were incorporated into WO_3 by the simple hydrogen thermal treatment approach. The lack of oxygen atoms changed the way in which the heterointerface is electronically structured and coordinated. Specifically, the W 5d band was affected by increasing electron densities caused by Ovs anchored with S atoms, forming a close interface connection. This, in turn, acted as a channel for interfacial photogenerated charge transfer. Through femto-second transient absorption spectroscopy (fs-TAS), it was presumed that the electron trapping states caused by Ovs may trigger additional ways of transporting charges, which led to an increase in charge separation efficiency. In addition, Ovs promoted light absorption, realizing the modulation of thermodynamic parameters of the photo-catalytic process. The photocatalytic degradation perform-ance of the optimal sample showed significant enhancement, which was not only 35.5 and 3.9 times higher than that of the single component of WO_3 with Ovs and In_2S_3, respectively. Meanwhile, it was found that the activity of the composite photocatalyst was superior to that of WO_3/In_2S_3 without the introduction of Ovs. These findings will help with the development of new photocatalysts that have even greater efficiency.

Results and Discussion

Design of WO₃-Ov/In₂S₃ Photocatalysts

WO_3 nanoparticles with Ovs (WO_3-Ov) were prepared by annealing pristine WO_3 nanoparticles in 450 °C for 1 h at 5 % H_2/Ar atmosphere. In_2S_3 was subsequently grown on the surface of WO_3-Ov via a hydrothermal method. The syn-thesis process of WO_3-Ov/In_2S_3 heterojunction structure is illustrated in Figure 1a. The obtained samples with different contents of In_2S_3 are denoted as $W_{Ov}In1$, $W_{Ov}In2$, and $W_{Ov}In3$, while the heterojunction samples of In_2S_3 grown on pristine WO_3 nanoparticles are denoted as WIn1, WIn2, and WIn3. It can be seen from field emission scanning electron microscopy (FESEM) (Figure S1) that the size of pristine WO_3 nanoparticles is ~100 nm. After the introduction of Ovs, the morphology remains unchanged. FESEM images show that, as the amount of In_2S_3 increases, both the surface
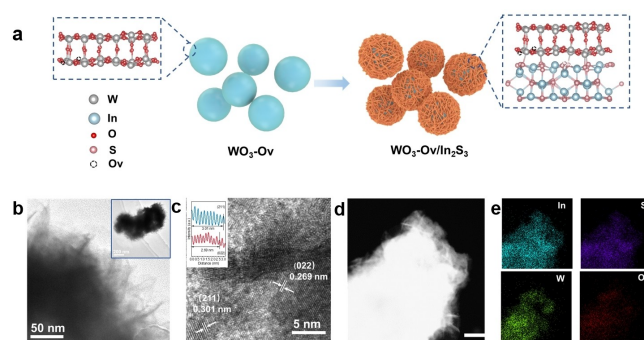

Figure 1. Schematic illustration and micromorphology. a) Schematic illustration of the preparation process of WO_3-Ov/In_2S_3 heterojunction structure. b) TEM images of $W_{Ov}In2$. c) HRTEM image of $W_{Ov}In2$. The inset figure is the corresponding line profiles. d) HAADF image of $W_{Ov}In2$. e) Elemental mapping of In, S, W, and O in the $W_{Ov}In2$ sample. The scale bar is 100 nm.

of WO_3-Ov/In_2S_3 (Figure S2) and WO_3/In_2S_3 samples (Fig-ure S3) are covered with increasing amount of hierarchical structures. Furthermore, transmission electronic microscopy (TEM) confirms the hierarchical architecture of $W_{Ov}In2$ (inset of Figure 1b). Figure 1b illustrates that the hierarch-ical In_2S_3 is composed of plenty of nanoflakes assembled on the surface of the WO_3-Ov nanoparticle. It should be noted that this hierarchical morphology can provide a large number of active sites to participate in the photocatalytic reaction, which benefits the photocatalytic performances. In high solution TEM images (HRTEM, Figure 1c), In_2S_3 displays clear lattice fringes with an interlayer spacing of 0.269 and 0.301 nm, which can be assigned to the (022) and (211) crystal planes of β-In_2S_3, respectively. Inset of Fig-ure 1c presents the profiles of corresponding lattice fringes. Furthermore, high angle annular dark-field (HAADF) image of $W_{Ov}In2$ (Figure 1d) and corresponding elemental mapping images of In, S, W, and O (Figure 1e) reveal that hierarchical In_2S_3 with uniform composition are anchored on WO_3-Ov nanoparticles.

Characterization of WO₃-Ov/In₂S₃ Photocatalysts

To detect the unpaired electrons in WO_3-Ov, electron paramagnetic resonance (EPR) measurement was carried out. As shown in Figure 2a, the g value at 2.003 corresponds to unpaired electrons in the Ov site.[2] It is apparent that after the hydrogen thermal reduction process, the signal area at $g = 2.003$ exhibits significant enhancement, confirm-ing that a considerable number of Ovs were introduced to WO_3 with this simple method. X-ray diffraction (XRD) was adopted to figure out the crystal structure of WO_3-Ov, In_2S_3, and WO_3-Ov/In_2S_3. The peaks of WO_3-Ov can be well indexed to the monoclinic phase (JCPDS card no. 71–2141), which is consistent with pristine WO_3 (Figure S4). It can be concluded that the hydrogen thermal annealing keeps WO_3 in its pristine crystal phase. As shown in Figure 2b, the diffraction peaks of In_2S_3 can be indexed to tetragonal β-In_2S_3 (JCPDS card no. 84–1385). XRD patterns of WO_3-Ov/
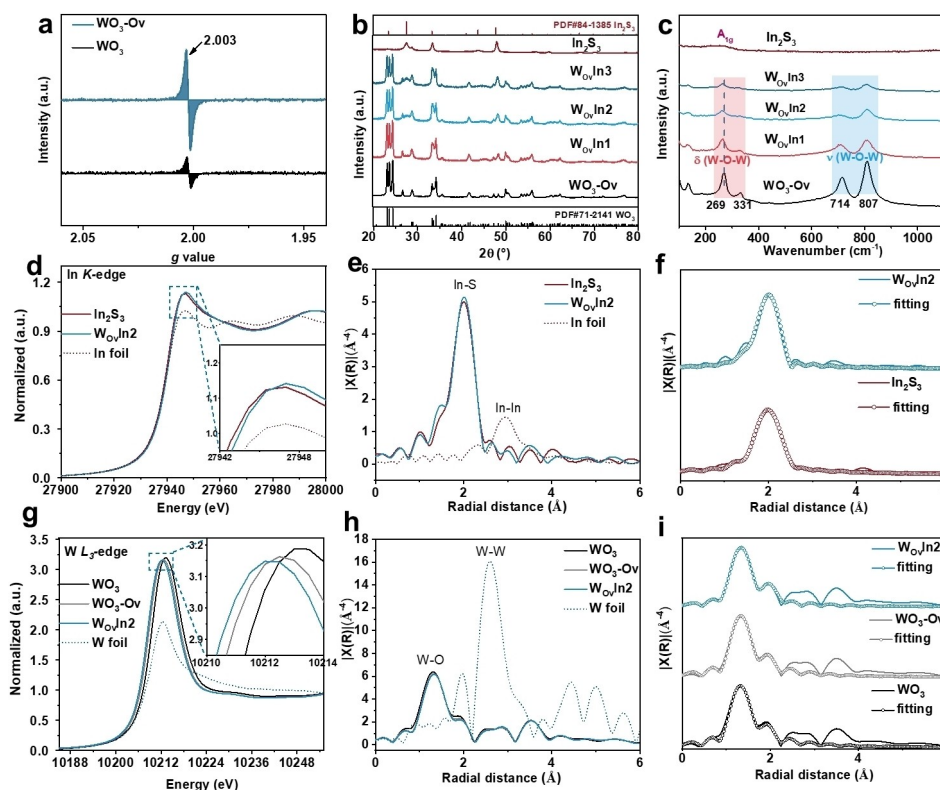
Figure 2. Crystal structures and local chemical environmental characterizations of WO_3-Ov/In_2S_3. a) EPR spectra of WO_3 and WO_3-Ov. b) XRD patterns and c) Raman spectra of WO_3-Ov, In_2S_3, and WO_3-Ov/In_2S_3 samples. In K-edge d) XANES spectra, e) EXAFS spectra and f) EXAFS fitting spectra of In_2S_3 and $W_{Ov}In2$. W L_3-edge g) XANES spectra, h) EXAFS spectra and i) EXAFS fitting spectra of WO_3, WO_3-Ov and $W_{Ov}In2$.

In_2S_3 verify the successful synthesis of WO_3-Ov/In_2S_3 heterojunction. Moreover, with increasing content of In_2S_3 in WO_3-Ov/In_2S_3 heterojunction, the peak intensities of the In_2S_3 phase increase accordingly. The matching of the XRD peaks of WO_3-Ov/In_2S_3 to those of the combination of WO_3-Ov and In_2S_3 single component indicates that the crystal structure is not altered in the hybridization process. Similarly, XRD patterns of WIn1, WIn2, and WIn3 (Figure S4) also confirm the successful construction of WO_3/In_2S_3 heterojunctions. Raman spectra were conducted to investigate the structural information of the heterojunction. As shown in Figure 2c, Raman peaks of WO_3-Ov at 714 and 807 cm^{-1} can be assigned to the stretching vibrations of longer and shorter W–O–W bonds in WO_6 octahedron units, respectively. The peaks at 269 and 331 cm^{-1} are attributed to the bending vibrations of the bridging oxygen atoms in W–O–W.[18] In comparison, the main Raman peak of WO_3-Ov demonstrates obvious peak shifting and broadening compared with pristine WO_3 (Figure S5a), which is related to the deficiency of oxygen atoms and nonstoichiometry on the WO_3 surface.[19] The Raman spectra of In_2S_3 show a distinct peak at 306 cm^{-1}, which is associated with A_{1g} mode of β-In_2S_3.[20] The Raman spectra of WO_3-Ov/In_2S_3 are composed of oscillation peaks of WO_3-Ov and In_2S_3. It can be observed that all the peaks in WO_3-Ov/In_2S_3 shift to lower wavenumber compared with pristine WO_3-Ov, confirming the chemical bonding effect between heterointerface.[21–23] Raman spectra of WO_3/In_2S_3 are de-

picted in Figure S5b, where the main peak of WO_3/In_2S_3 shows a similar shift tendency compared with pristine WO_3. X-ray photoelectron spectroscopy (XPS) was performed to examine the valence state change of the elements in WO_3-Ov/In_2S_3 heterojunctions. XPS survey spectra (Figure S6) show the existence of W, O, In, and S in this heterojunction. Pristine In_2S_3 demonstrates two peaks located at 444.8 and 452.3 eV, which correspond to In $3d_{5/2}$ and $3d_{3/2}$, respectively (Figure S7a). After hybridization, these two peaks shift to higher binding energies. Moreover, W 4f XPS spectra of WO_3-Ov (Figure S7b) demonstrate two peaks at 37.6 and 35.5 eV.[18,24] W 4f peaks of WO_3-Ov/In_2S_3 samples show a negative shift compared with WO_3-Ov. After conjunction, S 2p XPS (Figure S8a) shows that S $2p_{3/2}$ and $2p_{1/2}$ locate at 161.7 and 162.9 eV, respectively.[25–26] Whereas, in these heterojunctions, S $2p_{3/2}$ and $2p_{1/2}$ shift to higher binding energy. The positive shifts of In 3d and S 2p XPS peaks indicate the loss of electrons in In_2S_3 upon conjunction.

Meanwhile, O1s XPS (Figure S8b) demonstrates that the lattice O of WO_3-Ov/In_2S_3 moves to lower binding energy compared with WO_3-Ov, showing the same peak shifting tendency as W 4f XPS after hybridization. It can be concluded from W 4f and O 1s XPS that WO_3-Ov accepts electrons after being in contact with In_2S_3. Further, it can be presumed that upon the contact of WO_3-Ov and In_2S_3 with different E_f, electrons spontaneously transfer from In_2S_3 to WO_3-Ov until E_f is equilibrated at the heterointerface. Consequently, the flow of electrons results in the formation

of an internal electric field between the heterointerface of the two semiconductors, pointing from In_2S_3 to WO_3-Ov. XPS of WO_3-Ov and WO_3 are exhibited in Figure S9 and S10 to compare their chemical states. XPS of WO_3/In_2S_3 are shown in Figure S11, the detailed analysis can be found in Supporting Information.

The electronic structure and coordination environment of In and W before and after conjunction were investigated by X-ray absorption near edge structure (XANES). It can be seen that In K pre-edge peak position of $W_{Ov}In2$ centers at a higher energy than that of In_2S_3, indicating that the In element in $W_{Ov}In2$ possesses higher valence state than that in In_2S_3 (Figure 2d),[27–28] which is consistent with the In 3d XPS results. Fourier-transformed extended X-ray absorption fine structure (EXAFS) (Figure 2e) was obtained to acquire quantitative structural parameters. It can be noticed that the near-edge absorption energy of $W_{Ov}In2$ shifts to higher R direction (2.02 Å) with increased intensity compared with In_2S_3 (1.99 Å), implying that the chemical bonding character of the In_2S_3 has been changed after the hybridization. Figure 2f presents the fitting result of the extended In K-edge. Table S1 summarizes the quantitative structural parameters fitting result of the extended In K-edge. W L_3-edge XANES spectra (Figure 2g) shows that the white line intensity of as prepared WO_3-Ov is slightly lower than pristine WO_3. The weaker white line absorption peak is related to the increase of W 5d band electron densities in WO_3-Ov.[29–30] After the growth of In_2S_3, $W_{Ov}In2$ shows a lower intensity peak, revealing the higher average electron density and the decrease of oxidation states of W compared with WO_3-Ov, strongly verifying that WO_3-Ov accept electrons in this $W_{Ov}In2$ heterojunction.[29] EXAFS spectra of W L_3-edge for WO_3, WO_3-Ov and $W_{Ov}In2$ are displayed in Figure 2h. EXAFS curve fitting of W-L_3 (Figure 2i) shows that compared with WO_3, the coordination number in WO_3-Ov decreases, which is related to the deficiency of oxygen atoms. Moreover, as for $W_{Ov}In2$, apart from W–O bond, W–S bond (2.39 Å) as chemical covalent bond forms in $W_{Ov}In2$. It can be verified that the growth of In_2S_3 changes the W chemical bonding environment in WO_3-Ov samples. The fitting parameters of W L_3-edge EXAFS are summarized in Table S2. The wavelet transform contour plots of In K-edge weighted EXAFS for In_2S_3 and $W_{Ov}In2$ (Figure S12), and W L_3-edge for WO_3, WO_3-Ov and $W_{Ov}In2$ (Figure S13) also highlight minor differences in $W_{Ov}In2$ and the two single components.[31] The above results provide evidence that, after the combination, the electrons transfer from In_2S_3 to WO_3-Ov. And the W–S chemical bonding between WO_3-Ov and In_2S_3 is formed at the interface, which may provide an electron transport pathway during photocatalytic process. The microscopic environment and local electronic structure of WIn2 samples are depicted in Supporting Information (Figures S14–S17, Table S3 and S4). The neighboring structure around W atoms and In atoms of WIn2 shows differences compared with WO_3 and In_2S_3 components. k^3-weighted EXAFS data and fit data are shown in Figure S18 and Figure S19. Figure S20 shows crystal structure models of In_2S_3 and WO_3 used in EXAFS fitting.

Band Structure Analysis

The light absorption property of the photocatalysts was tested by UV–Vis diffuse reflectance spectroscopy (DRS). As shown in Figure S21, compared with pristine WO_3, WO_3-Ov shows evidently enhanced photo absorption in the visible region. After hybridization, WO_3-Ov/In_2S_3 heterojunctions show absorption edge from 550 to 580 nm (Figure S22a), which is similar to In_2S_3. The absorption abilities of WO_3-Ov/In_2S_3 heterojunctions is stronger than that of WO_3/In_2S_3 heterojunctions (Figure S22b), which is beneficial to their photocatalytic properties. The optical photographs of WO_3-Ov/In_2S_3 heterojunctions and WO_3/In_2S_3 heterojunctions are displayed in Figure S23a and S23b, respectively, showing that the existence of Ovs deepens the color of the heterojunctions.

Tauc plot can be obtained based on UV–Vis DRS and Kubelka–Munk equation to analyze the band gap value (E_g) of the semiconductors. As shown in Figure S24, E_g of WO_3-Ov and WO_3 is estimated to be 2.71 and 2.89 eV, respectively, which verifies that the introduction of Ov can slightly lower E_g. In addition, E_g of In_2S_3 is calculated to be 2.17 eV. Ultraviolet photoelectron spectroscopy (UPS) was carried out to assess the band structure of the semiconductor photocatalyst. As presented in Figure S25a, the secondary cutoff binding energy (E_{cutoff}) is measured to be 17.01 eV for WO_3-Ov. By applying the equation: $\Phi = h\nu - E_{cutoff}$, the work function (Φ) of WO_3-Ov can be calculated to be 4.21 eV. Hence, the E_f of WO_3-Ov can be determined as -0.19 V (vs. NHE). As shown in Figure S25b, E_{cutoff} of In_2S_3 was measured to be 17.36 eV, Φ and E_f of In_2S_3 can be estimated to be 3.86 eV and -0.54 V (vs. NHE), respectively. Mott–Schottky plots show positive slopes, indicating the n-type behavior of WO_3-Ov (Figure S26a) and In_2S_3 (Figure S26b).[32] The conduction band potential (E_{CB}) can be evaluated by Mott–Schottky plots. The flat band potentials (E_{fb}) of WO_3-Ov and In_2S_3 are estimated to be -0.09 and -0.65 V (vs. NHE), respectively.[33] It is confirmed by previous studies that E_{CB} of n-type semiconductor is ~0.2 V negative than the E_{fb}.[22] Therefore, the E_{CB} of WO_3-Ov and In_2S_3 is estimated to be -0.29 and -0.85 V (vs. NHE), respectively.

Potential of valence band (E_{VB}) can be obtained according to the equation of $E_g = E_{CB} - E_{VB}$,[34] which can be estimated to be 2.42 and 1.32 V (vs. NHE) for WO_3-Ov and In_2S_3, respectively. Figure 3a displays the detailed band structures of WO_3-Ov and In_2S_3 photocatalysts. EPR measurements were performed to further probe the reactive species in photocatalytic reactions, where 5,5-dimethyl-l-pyrroline N-oxide (DMPO) was adopted as a spin-trapping agent. Under light irradiation, hydroxyl (·OH) and superoxide (·O_2^-) radicals can be detected. As presented in Figure 3b and 3c, there is no signal observed under dark condition. Once irradiated by light, WO_3-Ov is more favorable for generating ·OH$^-$ rather than ·O_2^-, while In_2S_3 promotes the production of ·O_2^- instead of ·OH$^-$. These can be attributed to the fact that the VB position of WO_3-Ov is more positive than the potential of H_2O/·OH and CB position of In_2S_3 is more negative than the potential of O_2/
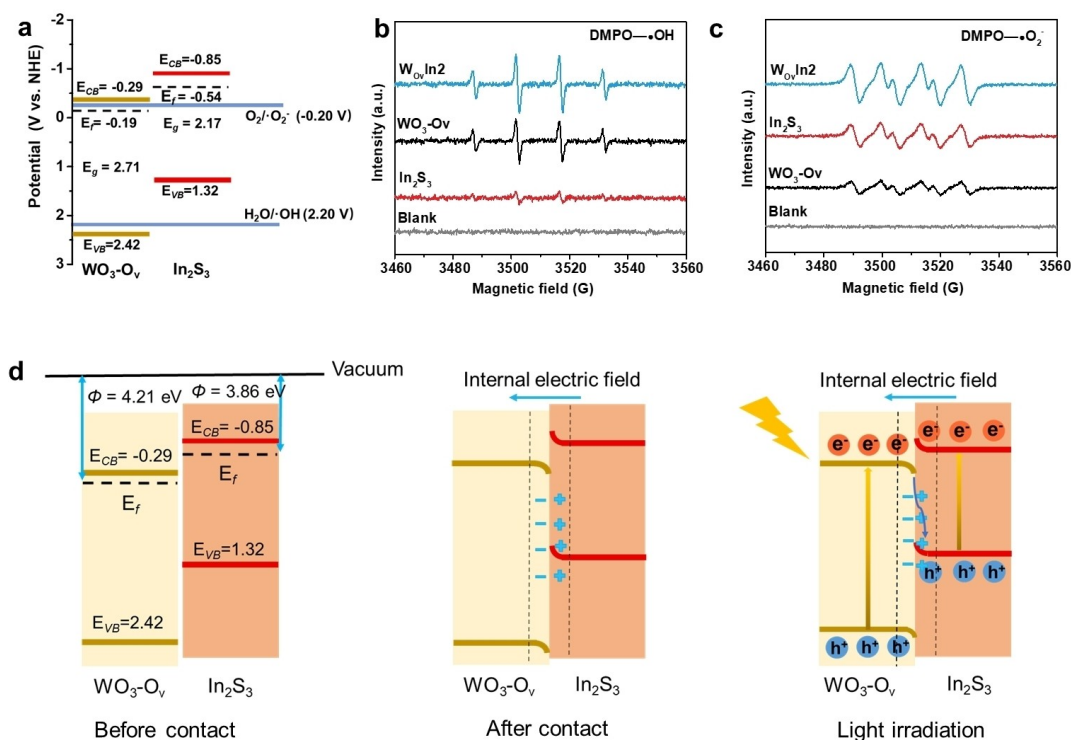
Figure 3. Band alignment and charge transport way at the heterointerface of WO$_3$-Ov/In$_2$S$_3$. a) Band alignment of WO$_3$-Ov/In$_2$S$_3$. EPR spectra of b) DMPO-•OH and c) DMPO-•O$_2^-$ in the presence of In$_2$S$_3$, WO$_3$-Ov, and W$_{Ov}$In2, respectively. d) The photocatalytic process of WO$_3$-Ov/In$_2$S$_3$ heterojunction under solar light irradiation.

•O$_2^-$.[26,35–37] In WO$_3$-Ov/In$_2$S$_3$ heterojunction structure, the recombination of photogenerated holes and electrons is inhibited effectively, which enables higher amount of photogenerated holes and electrons to oxidize H$_2$O and reduce O$_2$, respectively, causing the enhanced signal of •O$_2^-$ and •OH compared with the individual photocatalysts.[38–39] Moreover, in situ irradiation X-ray photoelectron spectroscopy (ISI-XPS) directly shows the transfer of photogenerated electrons from WO$_3$-Ov to In$_2$S$_3$ under light irradiation (Figure S27a and S27b), the detailed analysis can be found in Supporting Information. The results of EPR and ISI-XPS strongly verify the type of S-scheme heterojunction of WO$_3$-Ov/In$_2$S$_3$. The charge transfer route in this S-scheme heterojunction can be proposed based on the above experiments and calculation results. As shown in Figure 3d, when WO$_3$-Ov and In$_2$S$_3$ contact together, an intimate interface forms. Due to the difference of E$_f$ between the two semiconductors, electrons will spontaneously transfer from In$_2$S$_3$ with higher E$_f$ to WO$_3$-Ov with lower E$_f$ until E$_f$ at the interface reaching equilibrium. Due to the redistribution of electrons on the interface of WO$_3$-Ov and In$_2$S$_3$, the band alignment near the interface changes correspondingly, and an internal electric field is built. In details, WO$_3$-Ov with electrons accumulation shows downward band bending at the interface, while In$_2$S$_3$ with electron loss shows upward band bending. When irradiated by the light, electrons in VB absorb photon energy and jump into CB, causing the photogenerated electrons and holes in CB and VB, respectively. With the joint effect of internal electric field,

band bending at the interface and Coulomb interaction, the photogenerated electrons in CB of WO$_3$-Ov tend to transfer to VB of In$_2$S$_3$ and combine with the holes. Through this pathway, the photogenerated carriers with low redox potentials merge, leaving the carriers with higher redox abilities separated apart, which significantly improves the efficiency of photocatalysis. Band structure of WO$_3$/In$_2$S$_3$ is analyzed in details in the Supporting Information (Figure S28 and S29).

Photocatalytic and Photoelectrochemical Performance

To evaluate the photocatalytic performance of the heterojunction, Rhodamine B (RhB) degradation property was tested. As shown in Figure 4a, under the irradiation of visible light, WO$_3$-Ov/In$_2$S$_3$ composites show significantly enhanced RhB photocatalytic degradation rate compared with pristine In$_2$S$_3$. Furthermore, the pseudo-first-order equation was utilized to quantitatively evaluate the degradation kinetics of RhB and the fitting curves are illustrated in Figure 4b. It can be seen that W$_{Ov}$In2 exhibits the highest K values (0.071) toward RhB degradation, followed by W$_{Ov}$In3 (0.058) and W$_{Ov}$In1 (0.044). Notably, W$_{Ov}$In2 shows the optimal performance, which is 8-folds higher than pristine In$_2$S$_3$. The photocatalytic RhB degradation performance of WO$_3$/In$_2$S$_3$ hybridizations is also provided in Figure S30. Pseudo first-order kinetics fitting of RhB degradation of WO$_3$/In$_2$S$_3$ composites is depicted in Figure S31. In order to
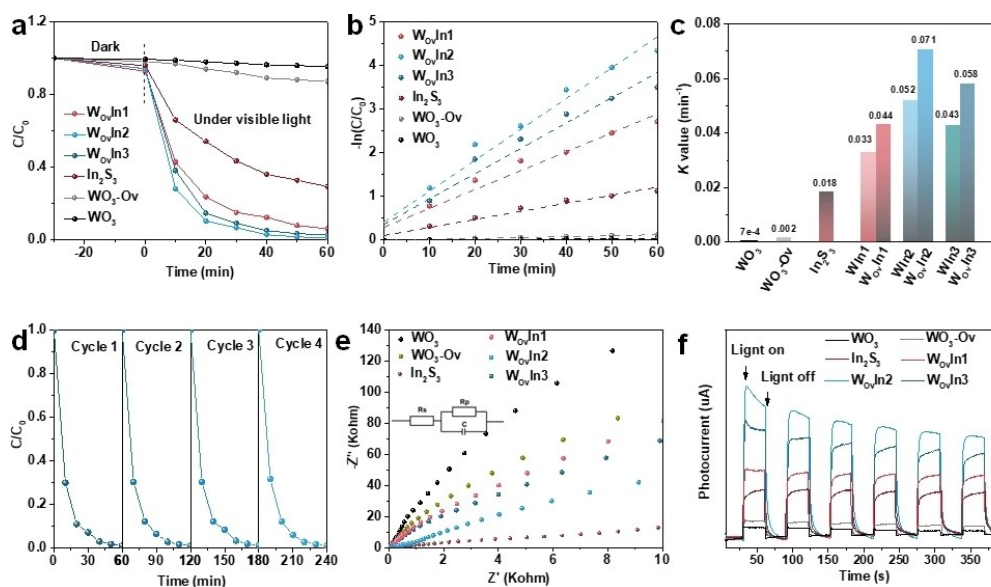
Figure 4. Enhancement in photocatalytic and photoelectrochemical performance after Ovs implantation. a) Photocatalytic degradation of RhB under visible-light irradiation over WO_3, WO_3-Ov, In_2S_3 and WO_3-Ov/In_2S_3 samples. b) Pseudo first-order kinetics fitting. c) Comparison of rate constants (K, min^{-1}) for different samples. d) Stability of photocatalytic RhB degradation of W_{Ov}In2 sample. e) EIS spectra of WO_3, WO_3-Ov, In_2S_3 and WO_3-Ov/In_2S_3 samples. f) Transient photocurrent spectra of WO_3, WO_3-Ov, In_2S_3 and WO_3-Ov/In_2S_3 samples.

compare the rate constants (K, min^{-1}) for WO_3-Ov/In_2S_3 and WO_3/In_2S_3, a histogram is depicted in Figure 4c. The photocatalytic RhB degradation abilities of the WO_3-Ov/In_2S_3 heterojunctions are higher than those of WO_3/In_2S_3 composites with the same In_2S_3 content. It can be presumed that the composites with specific electron transfer channels can remarkably improve the photocatalytic performance. Afterwards, the photocatalytic performance of W_{Ov}In2 was tested for 4 cycles to study its stability. Figure 4d demonstrates that there is no decay during the 4 cycles, revealing the high stability of W_{Ov}In2 S-scheme photocatalyst. The Brunauer–Emmett–Teller (BET) surface areas of all the photocatalysts are summarized in Table S5. K values after normalizing the specific surface are demonstrated in Figure S32 to eliminate the effect of adsorption ability. It can be seen that the creation of Ovs boosts the intrinsic photocatalytic degradation performance and W_{Ov}In2 shows the optimal performance. Furthermore, the photocatalytic phenol degradation performance of the as prepared samples was investigated (Figure S33), the detailed discussions are illustrated in Supporting Information. Transient photocurrent response and electrochemical impedance spectroscopy (EIS) were carried out to study charge transfer and separation efficiency of the photocatalysts. Charge transfer resistance can be evaluated by the semicircle diameter of EIS (Figure 4e). W_{Ov}In2 shows the lowest interfacial charge transfer resistance, verifying the efficient separation of photogenerated carriers. As shown in Figure 4f, the photocurrent density of WO_3-Ov/In_2S_3 hybridizations is higher than that of In_2S_3 under light irradiation, indicating a higher light harvesting ability and lower carrier recombination rate. Transient photocurrent response of WO_3/In_2S_3 (Figure S34) shows that WIn2 possesses the highest photo response current among

WO_3/In_2S_3 composites. Photoluminescence (PL) spectra were collected to investigate the charge transfer and separation kinetics of the photocatalysts. As shown in Figure S35, compared with pristine In_2S_3, the PL emission intensity peaks of WO_3-Ov/In_2S_3 quenches, confirming an enhanced photogenerated carrier separation in WO_3-Ov/In_2S_3.[22] W_{Ov}In2 shows the weakest peak intensity, which can be attributed to the fast photogenerated electrons transfer from WO_3-Ov to In_2S_3 at the interface of the W_{Ov}In2. It can be explained that the fast electron transfer channel at the heterointerface of WO_3-Ov and In_2S_3 builds a more efficient nonradiative decay pathway.

Density Functional Theory (DFT) Calculations

In order to unveil the effect of Ovs in the photocatalytic reaction, the related DFT calculation was carried out. As shown in Figure 5a, the partial density of states (PDOS) of WO_3-Ov at E_f demonstrates increment compared with WO_3 without Ovs, and the metallicity of WO_3-Ov is enhanced. It can be manifested that the W-5d and S-3p orbital overlap and hybridize to form covalent bond. W–S chemical bonds at the heterointerface can act as specific "bridge" to accelerate charge transfer between In_2S_3 and WO_3-Ov. Moreover, to visualize the charge transfer at the WO_3/In_2S_3 interface, the calculated charge density difference was employed to trace the electron transfer behavior. The charge accumulation and depletion are denoted in yellow and blue regions, as shown in Figure 5b and Figure S36a, where substantial charge transfer at the WO_3-Ov /In_2S_3 interface can be observed.[22] From the Bader charge analysis,[40] In_2S_3 transfers $1.342\, e^-$ to WO_3-Ov, verifying that the charge
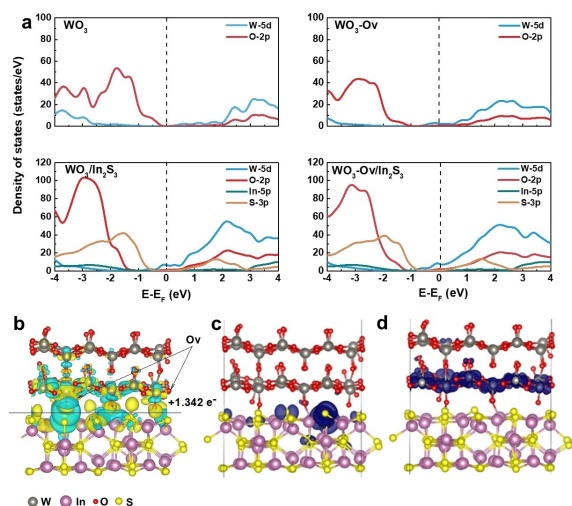
Figure 5. Calculated PDOS and differential charge density distribution of WO$_3$-Ov/In$_2$S$_3$. Partial density of states (PDOS) of a) WO$_3$, WO$_3$-Ov, WO$_3$/In$_2$S$_3$ and WO$_3$-Ov/In$_2$S$_3$. b) Differential charge density distribution of WO$_3$-Ov/In$_2$S$_3$ with Ovs. Isosurface level: 0.03 e/Bohr^3. Blue and yellow colors denote electron excess and deficiency area, respectively. Band-decomposed charge density distribution of c) VBM and d) CBM for WO$_3$-Ov/In$_2$S$_3$. The isosurface level is set as 0.001 e/Bohr^3.

and further efficiently steer the separation of photogenerated charge carriers. In order to further investigate the spatial distribution of photogenerated electrons and holes and visualize the impact of surface Ovs, additional first-principles calculations were conducted. Our findings indicate that WO$_3$-Ov generates photogenerated electrons from CB, which can subsequently be transferred to VB of In$_2$S$_3$ to combine with the photogenerated holes. The system of WO$_3$-Ov/In$_2$S$_3$ exhibits spatial separation between the valence band maximum (VBM, Figure 5c) and conduction band minimum (CBM, Figure 5d), effectively suppressing electron-hole recombination. Compared with band-decomposed charge density distribution of WO$_3$/In$_2$S$_3$ (Figure S37), the presence of Ovs leads to a greater electron localization of both VBM and CBM in the interface layer of the heterojunction, thereby forming a rapid charge transport channel between In$_2$S$_3$ and WO$_3$-Ov.

transfer at the interfaces makes the heterostructure structures tighter, and is consistent with the experimental results. The planar-averaged differential charge density as a function of z for WO$_3$-Ov/In$_2$S$_3$ is depicted in Figure S36b. The charge transfer at the heterointerface would subsequently induce the internal electric field in WO$_3$-Ov/In$_2$S$_3$ heterostructure

Fs-TAS Monitor Photogenerated Charge Dynamics

Furthermore, fs-TAS was performed to study the carrier dynamics (excited at 340 nm). As shown in Figure 6a, WO$_3$ exhibits a distinct positive photoinduced absorption band (400–500 nm), which can be attributed to the signal from photogenerated holes.[41–42] Compared with pristine WO$_3$, fs-TAS spectra of WO$_3$-Ov show significant difference (Figure 6b) with the appearance of negative absorption bands above 500 nm. The negative absorption bands result from the re-trapping of the photoexcited electrons from CB to vacancy centers,[42] indicating the kinetic behavior of photogenerated carriers can be effectively steered by Ovs defects.
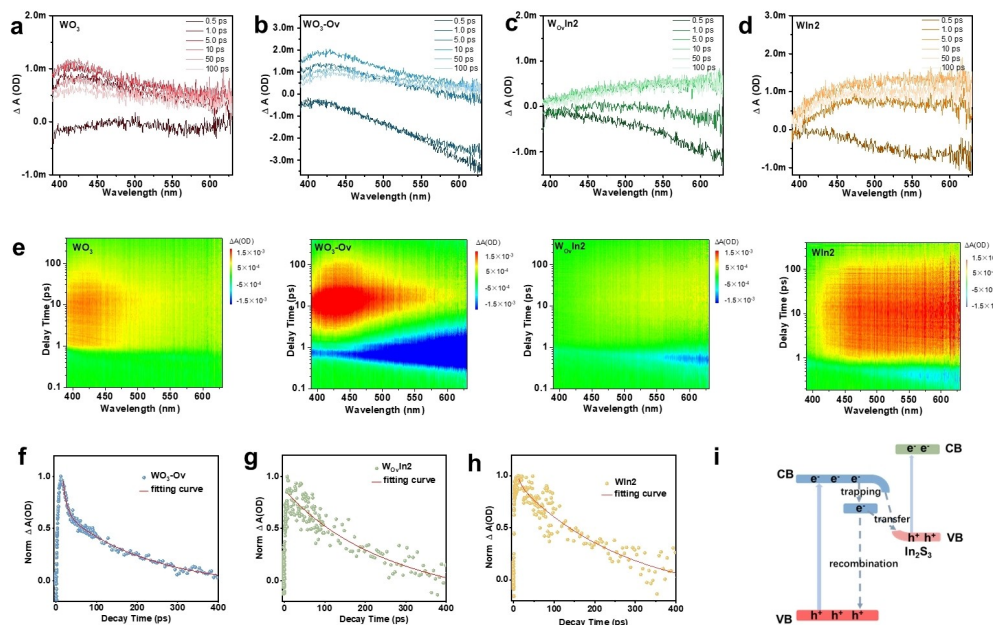
Figure 6. fs-TAS monitor the photogenerated charge dynamics. fs-TAS of a) WO$_3$, b) WO$_3$-Ov, c) W$_{Ov}$In2 and d) WIn2. e) Pseudo color plots of WO$_3$, WO$_3$-Ov, W$_{Ov}$In2 and WIn2. Normalized time profiles of fs-TAS at 428 nm of f) WO$_3$-Ov, g) W$_{Ov}$In2 and h) WIn2. i) Proposed photoinduced electron transfer and charge recombination route of WO$_3$-Ov/In$_2$S$_3$ heterojunction.

The fs-TAS spectra of $W_{Ov}In2$ are shown in Figure 6c. The intensity of negative photobleaching signal gradually increases in 0.5 ps, then decays within 5 ps, which is related to the kinetic behaviors of photogenerated electrons. The fs-TAS spectra of WIn2 demonstrate difference with $W_{Ov}In2$ (Figure 6d). Meanwhile, the pseudo color TA plots of WO_3, WO_3-Ov, $W_{Ov}In2$ and WIn2 are shown in Figure 6e, respectively. Furthermore, the decay curves of WO_3-Ov and $W_{Ov}In2$ at 598 nm were recorded and fitted by a two-exponential function to investigate the kinetics of photogenerated electrons (Figure S38), where the short time τ_1 and the long time τ_2 correspond to photogenerated electrons trapped by the shallow and deep trapping states, respectively.[43–44] Compared with WO_3-Ov ($\tau_1 = 0.65$ ps, $\tau_2 = 6.03$ ps), the lifetime of $W_{Ov}In2$ decreases ($\tau_1 = 0.39$ ps, $\tau_2 = 3.16$ ps), which can be inferred that an additional channel for electron transfer exists at the interface between WO_3-Ov and In_2S_3, accelerating the relaxation process of electrons. To estimate the decay kinetics of photogenerated holes, time profiles of fs-TAS at 428 nm were probed. Compared with WO_3-Ov ($\tau_{ave} = 194.4$ ps) (Figure 6f), the average decay lifetime (τ_{ave}) of $W_{Ov}In2$ is prolonged to 528.1 ps (Figure 6g), suggesting that photogenerated holes in the composite possess much longer lifetime and higher priority to participate in photo oxidation reactions.[45] As comparison, the τ_{ave} of WIn2 is 265.9 ps (Figure 6h), shorter than that of $W_{Ov}In2$, further suggesting the creation of Ovs prolongs the lifetime of the photo-induced holes, thus favoring the improvement in photocatalytic activity. The fitting results are summarized in Table S6 and S7, which confirms the formation of S-scheme charge transfer between WO_3-Ov and In_2S_3. Based on the above analysis, the mechanism of Ovs in the S-scheme heterojunction can be proposed, as depicted in Figure 6i. Ovs can generate impurity trap states in WO_3-Ov which partially trap photogenerated electrons, thus inhibit direct recombination of the photogenerated electrons and holes. After hybridizing with In_2S_3, a new interfacial electron transfer pathway may be generated, the electron transfer and migration can be promoted by the internal electric field at the interface.[46] The rapid electron trapping as well as the fast charge separation at the interface of WO_3-Ov/In_2S_3 suppress electron-hole recombination. In addition, the existence of Ovs narrows the band gap of WO_3-Ov, resulting in the enhancement of light absorption and the increased number of photogenerated carriers to participate the reaction.

Conclusions

In this work, WO_3-Ov/In_2S_3 S-scheme heterojunction photocatalysts were successfully synthesized. The photocatalytic degradation performance of WO_3-Ov/In_2S_3 S-scheme heterojunction was superior to that of single-component (35.5 and 3.9 times higher than WO_3-Ov and In_2S_3, respectively.) and WO_3/In_2S_3 heterojunction. The results of experimental characterizations and DFT calculations revealed that the microscopic environment and local electronic structure of S-scheme heterointerface were well engineered by Ovs. Mean-while, Ovs favor the formation of a close interface connection. The influence of Ovs on charge transfer dynamics was investigated by employing fs-TAS. Ovs-induced trap states efficiently steered charge separation and triggered rapid charge transport channels at the heterointerface. Furthermore, Ovs improved light absorption, allowing for more photogenerated carriers. As a result, our study may contribute to a better understanding of Ov and the development of alternative S-scheme photocatalysts for advanced applications.

Conflict of Interest

The authors declare no conflict of interest.

Data Availability Statement

The data that support the findings of this study are available from the corresponding author upon reasonable request.

[1] M. Cai, Z. Wu, Z. Li, L. Wang, W. Sun, A. A. Tountas, C. Li, S. Wang, K. Feng, A.-B. Xu, S. Tang, A. Tavasoli, M. Peng, W. Liu, A. S. Helmy, L. He, G. A. Ozin, X. Zhang, *Nat. Energy* **2021**, *6*, 807–814.

[2] F. Chen, T. Ma, T. Zhang, Y. Zhang, H. Huang, *Adv. Mater.* **2021**, *33*, 2005256.

[3] L. Zhou, J. M. P. Martirez, J. Finzel, C. Zhang, D. F. Swearer, S. Tian, H. Robatjazi, M. Lou, L. Dong, L. Henderson, P. Christopher, E. A. Carter, P. Nordlander, N. J. Halas, *Nat. Energy* **2020**, *5*, 61–70.

[4] X. Sun, X. Zhang, Y. Xie, *Matter* **2020**, *2*, 842–861.

[5] Z. Zhang, J. Huang, Y. Fang, M. Zhang, K. Liu, B. Dong, *Adv. Mater.* **2017**, *29*, 20170306.

[6] R. Chen, S. Pang, H. An, J. Zhu, S. Ye, Y. Gao, F. Fan, C. Li, *Nat. Energy* **2018**, *3*, 655–663.

[7] D. Zhao, Y. Wang, C.-L. Dong, Y.-C. Huang, J. Chen, F. Xue, S. Shen, L. Guo, *Nat. Energy* **2021**, *6*, 388–397.

[8] L. Pan, M. Ai, C. Huang, L. Yin, X. Liu, R. Zhang, S. Wang, Z. Jiang, X. Zhang, J. J. Zou, W. Mi, *Nat. Commun.* **2020**, *11*, 418.

[9] P. Xia, S. Cao, B. Zhu, M. Liu, M. Shi, J. Yu, Y. Zhang, *Angew. Chem. Int. Ed.* **2020**, *59*, 5218–5225.

Angew. Chem. Int. Ed. **2024**, *63*, e202405756 (8 of 9)

© 2024 The Authors. Angewandte Chemie International Edition published by Wiley-VCH GmbH

[10] F. Xu, K. Meng, B. Cheng, S. Wang, J. Xu, J. Yu, *Nat. Commun.* **2020**, *11*, 4613.

[11] Q. Xu, L. Zhang, B. Cheng, J. Fan, J. Yu, *Chem* **2020**, *6*, 1543–1559.

[12] L. Zhang, J. Zhang, H. Yu, J. Yu, *Adv. Mater.* **2022**, *34*, 2107668.

[13] M. Gerosa, F. Gygi, M. Govoni, G. Galli, *Nat. Mater.* **2018**, *17*, 1122–1127.

[14] Y. Bo, H. Wang, Y. Lin, T. Yang, R. Ye, Y. Li, C. Hu, P. Du, Y. Hu, Z. Liu, R. Long, C. Gao, B. Ye, L. Song, X. Wu, Y. Xiong, *Angew. Chem. Int. Ed.* **2021**, *60*, 16085–16092.

[15] D. Knez, G. Drazic, S. K. Chaluvadi, P. Orgiani, S. Fabris, G. Panaccione, G. Rossi, R. Ciancio, *Nano Lett.* **2020**, *20*, 6444–6451.

[16] T. Hou, Y. Xiao, P. Cui, Y. Huang, X. Tan, X. Zheng, Y. Zou, C. Liu, W. Zhu, S. Liang, L. Wang, *Adv. Energy Mater.* **2019**, *9*, 1902319.

[17] M. Kim, B. Lee, H. Ju, J. Y. Kim, J. Kim, S. W. Lee, *Adv. Mater.* **2019**, *31*, 1903316.

[18] T. Zheng, W. Sang, Z. He, Q. Wei, B. Chen, H. Li, C. Cao, R. Huang, X. Yan, B. Pan, S. Zhou, J. Zeng, *Nano Lett.* **2017**, *17*, 7968–7973.

[19] H. Kong, H. Yang, J. S. Park, W. S. Chae, H. Y. Kim, J. Park, J. H. Lee, S. Y. Choi, M. Park, H. Kim, Y. Song, H. Park, J. Yeo, *Adv. Funct. Mater.* **2022**, *32*, 2204106.

[20] J. Hou, S. Cao, Y. Sun, Y. Wu, F. Liang, Z. Lin, L. Sun, *Adv. Energy Mater.* **2017**, *8*, 1701114.

[21] J. Wang, D. Liu, H. Huang, N. Yang, B. Yu, M. Wen, X. Wang, P. K. Chu, X. F. Yu, *Angew. Chem. Int. Ed.* **2018**, *57*, 2600–2604.

[22] X. Wang, X. Wang, J. Huang, S. Li, A. Meng, Z. Li, *Nat. Commun.* **2021**, *12*, 4112.

[23] Y. Wang, Y. Tang, J. Sun, X. Wu, H. Liang, Y. Qu, L. Jing, *Appl. Catal. B* **2022**, *319*, 121893.

[24] Y. Ji, Y. Yang, S. K. Lee, G. Ruan, T. W. Kim, H. Fei, S. H. Lee, D. Y. Kim, J. Yoon, J. M. Tour, *ACS Nano* **2016**, *10*, 7598–7603.

[25] Y. He, H. Rao, K. Song, J. Li, Y. Yu, Y. Lou, C. Li, Y. Han, Z. Shi, S. Feng, *Adv. Funct. Mater.* **2019**, *29*, 1905153.

[26] Y. Yang, B. Cheng, J. Yu, L. Wang, W. Ho, *Nano Res.* **2023**, *16*, 4506–4514.

[27] E. Zhang, L. Tao, J. An, J. Zhang, L. Meng, X. Zheng, Y. Wang, N. Li, S. Du, J. Zhang, D. Wang, Y. Li, *Angew. Chem. Int. Ed.* **2022**, *61*, 202117347.

[28] B. Pan, G. Yuan, X. Zhao, N. Han, Y. Huang, K. Feng, C. Cheng, J. Zhong, L. Zhang, Y. Wang, Y. Li, *Small Sci.* **2021**, *1*, 210002.

[29] Y. Cui, X. Tan, K. Xiao, S. Zhao, N. M. Bedford, Y. Liu, Z. Wang, K.-H. Wu, J. Pan, W. H. Saputera, S. Cheong, R. D. Tilley, S. C. Smith, J. Yun, L. Dai, R. Amal, D.-W. Wang, *ACS Energy Lett.* **2020**, *5*, 3560–3568.

[30] Z. Sun, R. Huo, C. Choi, S. Hong, T.-S. Wu, J. Qiu, C. Yan, Z. Han, Y. Liu, Y.-L. Soo, Y. Jung, *Nano Energy* **2019**, *62*, 869–875.

[31] C. Pi, X. Li, X. Zhang, H. Song, Y. Zheng, B. Gao, A. Kizilaslan, P. K. Chu, K. Huo, *Small* **2022**, *18*, 2201137.

[32] K. Sivula, *ACS Energy Lett.* **2021**, *6*, 2549–2551.

[33] Y. Wei, N. Yang, K. Huang, J. Wan, F. You, R. Yu, S. Feng, D. Wang, *Adv. Mater.* **2020**, *32*, 2002556.

[34] S. Cao, B. Shen, T. Tong, J. Fu, J. Yu, *Adv. Funct. Mater.* **2018**, *28*, 1800136.

[35] X. Liu, Q. Zhang, D. Ma, *Solar RRL* **2020**, *5*.

[36] Y. Wang, X. Li, S. Liu, Y. Liu, T. Kong, H. Zhang, X. Duan, C. Chen, S. Wang, *ACS Catal.* **2022**, *12*, 2770–2780.

[37] C. Ling, X. Liu, M. Li, X. Wang, Y. Shi, J. Qi, J. Zhao, L. Zhang, *Appl. Catal. B* **2021**, *290*, 120051.

[38] J. Fu, Q. Xu, J. Low, C. Jiang, J. Yu, *Appl. Catal. B* **2019**, *243*, 556–565.

[39] Y. Li, W. Zhang, J. Niu, Y. Chen, *ACS Nano* **2012**, *6*, 5164–5173.

[40] W. Tang, E. Sanville, G. Henkelman, *J. Phys. Condens. Matter* **2009**, *21*, 084204.

[41] K. Kato, Y. Uemura, K. Asakura, A. Yamakata, *J. Phys. Chem. C* **2022**, *126*, 9257–9263.

[42] M. Sachs, J. S. Park, E. Pastor, A. Kafizas, A. A. Wilson, L. Francas, S. Gul, M. Ling, C. Blackman, J. Yano, A. Walsh, J. R. Durrant, *Chem. Sci.* **2019**, *10*, 5667–5677.

[43] Y. Li, Q. Wu, Y. Chen, R. Zhang, C. Li, K. Zhang, M. Li, Y. Lin, D. Wang, X. Zou, T. Xie, *Appl. Catal. B* **2021**, *290*, 120058.

[44] F. Liu, R. Shi, Z. Wang, Y. Weng, C. M. Che, Y. Chen, *Angew. Chem. Int. Ed.* **2019**, *58*, 11791–11795.

[45] C. Xing, G. Yu, J. Zhou, Q. Liu, T. Chen, H. Liu, X. Li, *Appl. Catal. B* **2022**, *315*, 121496.

[46] Z. Wei, W. Wang, W. Li, X. Bai, J. Zhao, E. C. M. Tse, D. L. Phillips, Y. Zhu, *Angew. Chem. Int. Ed.* **2021**, *60*, 8236–8242.